



On modeling quantum point contacts in quantum Hall systems

Prasoon Kumar  and Kyrylo Snizhko 

Univ. Grenoble Alpes, CEA, Grenoble INP, IRIG, PHELIQS, 38000 Grenoble, France

(Dated: 11th December 2025)

Quantum point contacts (QPC) are a key instrument in investigating the physics of edge excitations in the quantum Hall effect. However, at not-so-high bias voltage values, the predictions of the conventional point QPC model often deviate from the experimental data both in the integer and (more prominently) in the fractional quantum Hall regime. One of the possible explanations for such behaviors is the dependence of the tunneling between the edges on energy, an effect not present in the conventional model. Here we introduce two models that take QPC spatial extension into account: wide-QPC model that accounts for the distance along which the edges are in contact; long-QPC model accounts for the fact that the tunneling amplitude originates from a finite bulk gap and a finite distance between the two edges. We investigate the predictions of these two models in the integer quantum Hall regime for the energy dependence of the tunneling amplitude. We find that these two models predict opposite dependences: the amplitude decreasing or increasing away from the Fermi level. We thus elucidate the effect of the QPC geometry on the energy dependence of the tunneling amplitude and investigate its implications for transport observables.

I. INTRODUCTION

Quantum Hall (QH) effect is one of the most celebrated phenomena in condensed matter physics [1]. Beyond conductance quantization, its fractional version exhibits excitations with fractional charge [2–10] and anyonic statistics [11–17]. Such unconventional quasiparticle excitations might be useful for topological quantum computing [18].

The origin of the conductance quantization is the formation of chiral edge channels. These edge channels play a crucial role both in theoretical understanding and experimental investigations of the quantum Hall physics. Indeed, many theoretical predictions for the nature of quantum Hall excitations stem from the chiral Luttinger liquid description of those edge channels [19]. A significant fraction of quantum Hall experiments involves tunneling contacts at which quasiparticles can jump between different edges — quantum point contacts (QPCs) [4–6, 9, 10, 12–17, 20, 21]. Many advanced predictions have been verified through such experiments.

At the same time, experiments with a single QPC often show discrepancies with theoretical predictions: they agree at small values of the bias voltage, while at larger values (eV larger than the system temperature, $k_B T$, yet significantly smaller than the bulk gap) they show noticeable disagreement [20–22]. With QPC being such an important instrument, it is crucial to understand the origin of these discrepancies in order to understand the instrument's limitations.

One of the possible explanations for the discrepancies is the energy dependence of the tunneling amplitude. This dependence is generally expected to be highly non-universal: it may depend on the QPC geometry, impurities present in the sample etc. Here we attempt to investigate the energy dependence of the tunneling amplitude from basic theoretical considerations.

Figure 1 shows the basic setup for QPC experiments: The edges are in contact in a restricted region of space.

The tunneling is investigated by injecting current at source contacts and measuring the output current and noise at the drain contacts. In the conventional model, Fig. 2, the tunneling is assumed to happen at a single point described by an energy-independent tunneling amplitude. This point-QPC model is the standard model for describing QPCs in the quantum Hall effect (see Refs. [23–28] to mention but a few examples). The works that did consider realistic geometries of the QPC [29–31] focused on the effect of Coulomb interactions and ignored non-point tunneling.

In this paper, we introduce two models that account for different aspects of the realistic geometry of the QPC. The wide-QPC model shown in Fig. 4 accounts for an extended width of the QPC — the distance along which the two edges are in contact with each other. The long-QPC model shown in Fig. 6 accounts for the fact that the tunneling amplitude originates from a finite bulk gap and for a finite distance between the two edges, and models the effective tunneling barrier between the edges. The long-QPC model essentially models a small piece of the quantum Hall bulk in the spirit of the wire construction [32].

Throughout the paper we focus on $\nu = 1$ integer quantum Hall regime. We investigate the predictions of above two models and show that they predict drastically distinct energy dependences of the tunneling behavior. We compare the predictions of these models with those of the point-QPC model and with each other. We also provide their predictions for a number of transport quantities that can be measured.

The structure of the paper is as follows. In Sec. II, we remind the reader the Landauer-Büttiker formalism [33–35] and define the transmission function of the QPC — the key object for our consideration. In Sec. III, we remind the reader the point-QPC model and introduce our wide- and long-QPC models. We discuss a theoretical peculiarity of the point-limit of all the models in Sec. IV. In Sec. V, we explore the predictions of the three

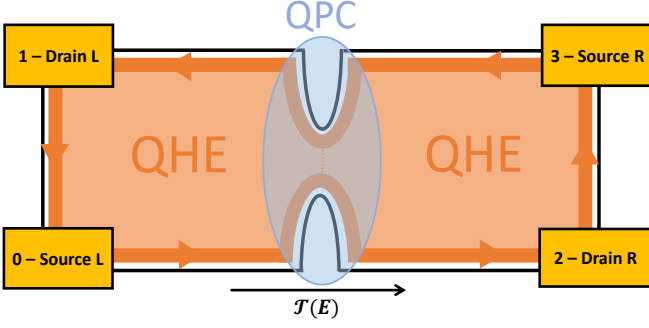


Figure 1. **Four-terminal setup of a quantum Hall QPC experiment.** The quantum Hall bulk supports a single chiral edge channel going around the sample (we focus on $\nu = 1$ integer quantum Hall regime). The edges from the opposite sides of the sample approach each other in one location — this is the QPC. Four Ohmic contacts are present in the sample, two (sources) are used to inject current into the chiral edge, two (drains) are used to extract the current that has passed through the QPC region. The key object for this paper's consideration is the energy-dependent transmission probability $\mathcal{T}(E)$: the probability for an excitation to be transmitted through the QPC without jumping to the other edge channel.

QPC models for realistic experiments. Finally, we provide some concluding remarks in Sec. VI.

II. TRANSMISSION FUNCTION

In this section, we introduce the setup of quantum Hall QPC experiments. We focus on the case of $\nu = 1$ integer quantum Hall regime and remind the reader how the Landauer–Büttiker formalism for transport in non-interacting mesoscopic systems applies to this system. In particular, we define the transmission function $\mathcal{T}(E)$, the key object for our consideration in the next sections.

The typical (four-terminal) setup of a quantum Hall QPC experiment is shown in Fig. 1. The sources are used to inject current into the chiral edge, as the drains are used to extract the current that has passed through the QPC region. The Landauer–Büttiker formalism [33–35], requires the knowledge of the scattering matrix that describes the probability amplitudes of electrons emitted by one contact to arrive at a different contact:

$$S = \begin{pmatrix} 0 & 1 & 0 & 0 \\ r_L & 0 & 0 & t_R \\ t_L & 0 & 0 & r_R \\ 0 & 0 & 1 & 0 \end{pmatrix} \begin{bmatrix} 0 - \text{Source L} \\ 1 - \text{Drain L} \\ 2 - \text{Drain R} \\ 3 - \text{Source R} \end{bmatrix}. \quad (1)$$

The above matrix involves the amplitudes $t_{R/L}(E)$ for an electron to be *transmitted* through the QPC without changing its edge and $r_{R/L}(E)$ for it to be *reflected* to the other edge. Unitarity of the S-matrix implies $|t_L(E)|^2 + |r_L(E)|^2 = 1$ and $|t_R(E)|^2 + |r_R(E)|^2 = 1$, from which it follows that $|t_R(E)|^2 = |t_L(E)|^2$. The probability of

being transmitted, $\mathcal{T}(E) = |t_L(E)|^2 = |t_R(E)|^2$, is called the transmission function.

We focus on the DC current I_2 extracted from Drain R, as well as the low-frequency noise of that current,

$$S_{22} = \left\langle \hat{I}(t)\hat{I}(t') + \hat{I}(t')\hat{I}(t) - 2\langle \hat{I}(t)\rangle\langle \hat{I}(t')\rangle \right\rangle_\omega, \quad (2)$$

where $\langle \dots \rangle_\omega$ is the Fourier component corresponding to $e^{i\omega(t-t')}$ of the time-domain correlation function. The Landauer–Büttiker formalism gives [33]

$$I_2 = \frac{e}{2\pi\hbar} \int dE \mathcal{T}(E) (f_L(E) - f_R(E)), \quad (3)$$

$$S_{22} = \frac{e^2}{\pi\hbar} \int dE \left\{ f_{\text{eq}}(E) (1 - f_{\text{eq}}(E)) + \mathcal{T}^2(E) f_L(E) (1 - f_L(E)) + (1 - \mathcal{T}(E))^2 f_R(E) (1 - f_R(E)) + \mathcal{T}(E) (1 - \mathcal{T}(E)) f_R(E) (1 - f_L(E)) + \mathcal{T}(E) (1 - \mathcal{T}(E)) f_L(E) (1 - f_R(E)) \right\}. \quad (4)$$

Here we assumed that the L and R sources are described by Fermi distributions $f_L(E) = f(E - \mu_L)$ and $f_R(E) = f(E - \mu_R)$, while the drains are in equilibrium with the sample and are defined by the equilibrium distribution $f_{\text{eq}}(E) = f(E - \mu)$, where $f(E) = (1 + e^{E/(k_B T)})^{-1}$. In what follows, we set $\mu = 0$.

Often the approximation of constant transmission is employed: $\mathcal{T}(E) = \mathcal{T}_0$. In this case, the above expressions simplify to

$$I_2|_{\mathcal{T}=\mathcal{T}_0} = \frac{e^2 V}{2\pi\hbar} \mathcal{T}_0, \quad (5)$$

$$S_{22}|_{\mathcal{T}=\mathcal{T}_0} = \frac{e^2}{\pi\hbar} \left[2k_B T + eV \mathcal{T}_0 (1 - \mathcal{T}_0) \left(\coth\left(\frac{eV}{2k_B T}\right) - \frac{2k_B T}{eV} \right) \right]. \quad (6)$$

Here we have taken $\mu_L - \mu_R = eV$ to be the bias voltage across the QPC.

Experiments often see behavior consistent with Eqs. (5–6) for small enough V , whereas at larger V deviations for this behavior (or its analogue for the fractional case) are observed both in the integer and (most prominently) in the fractional QH effect [4, 5, 20, 22]. One of the possible explanations is that the dependence of $\mathcal{T}(E)$ on the energy becomes important at larger values of the bias voltage. Below, we introduce several models, based on general considerations and investigate the dependence $\mathcal{T}(E)$ they predict, as well as its effect on I_2 and S_{22} .

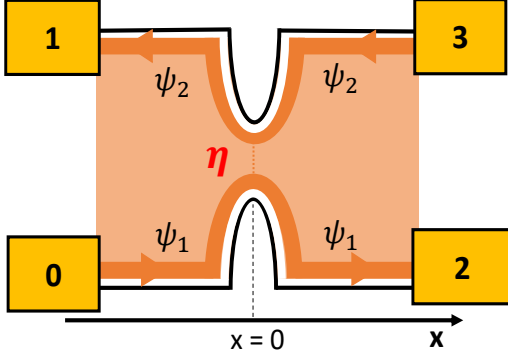


Figure 2. **Point-QPC model.** Two counter-propagating chiral edge modes approach each other at a single point, $x = 0$, which allows for tunneling of excitations between the edge modes.

III. ANALYTIC MODELS OF QUANTUM POINT CONTACT

In the previous section, we defined the key object for our consideration: the QPC transmission $\mathcal{T}(E)$. Here we introduce a number of phenomenological models that allow for predicting the energy dependence of $\mathcal{T}(E)$. We start by reminding the reader the standard point-QPC model. We then introduce two models that account for different aspects of the realistic geometry of the QPC: wide QPC and long QPC. We explain their physical meaning and calculate the $\mathcal{T}(E)$ for each of the models.

A. Point model

The standard model of QPC assumes that tunneling between the two edges happens at a single point, cf. 2. The model is described by the Hamiltonian

$$H_{\text{pqp}} = H_{\text{edge}} + H_{\text{tun-point}}, \quad (7)$$

$$H_{\text{edge}} = \int_{-\infty}^{+\infty} dx \left(-i\psi_1^\dagger v \partial_x \psi_1 + i\psi_2^\dagger v \partial_x \psi_2 \right), \quad (8)$$

$$H_{\text{tun-point}} = \eta \left(\psi_1^\dagger(x=0) \psi_2(x=0) + \text{h.c.} \right). \quad (9)$$

The edge Hamiltonian H_{edge} describes chiral fermionic channels ψ_1 and ψ_2 propagating to the right and to the left respectively. The tunneling Hamiltonian $H_{\text{tun-point}}$ describes electron transport between the two edges. Solving the scattering problem for H_{pqp} , one finds the transmission function

$$\mathcal{T}_{\text{pqp}}(E) = \mathcal{T}_{\text{pqp}}^{0 \rightarrow 2} = \left(\frac{1 - \frac{\eta^2}{4v^2}}{1 + \frac{\eta^2}{4v^2}} \right)^2. \quad (10)$$

The reader can find the details of the derivation in Appendix A.

The above result, though standard, warrants a few comments. First, note that $\mathcal{T}_{\text{pqp}}(E)$ does not depend on energy, which renders the transport predictions (5, 6) exact for this model.

Second, one naturally expects bigger values of η to lead to bigger tunneling (and, thus, smaller transmission) at the QPC. This intuition holds for $|\eta| \leq 2v$, at which $\mathcal{T}_{\text{pqp}}(E) = 0$ vanishes. For $|\eta| > 2v$, however, one again has $\mathcal{T}_{\text{pqp}}(E) > 0$. This indicates singular behavior of this model, which has been previously pointed out in the context of perturbative calculations [36]. The wide-QPC and long-QPC models considered below regularize this behavior in *distinct ways*. We will discuss this in more detail in Sec. V.

B. Wide model

In the previous section, we presented the conventional point-contact (point-QPC) model. A key assumption of the point-QPC model is that tunneling occurs at a single spatial point. However, quantum point contacts in real samples inevitably possess a finite tip width. Moreover, even in the most narrowly constructed QPCs, opposite QH edges are in contact over a width of the order of the magnetic length $l_B = \sqrt{\hbar/(eB)}$, as exemplified in Fig. 3. This challenges the point-like approximation and warrants an investigation of the effects of the finite width of the QPC.

To this end, we introduce the wide-QPC model, which incorporates a finite-width tunneling region between the chiral QH edge channels (Fig. 4). In this model, the two edge states, ψ_1 and ψ_2 propagate in opposite directions, as in Fig. 2. However, the tunneling happens over edge length L , and the tunneling amplitude is ζ :

$$H_{\text{wqp}} = H_{\text{edge}} + H_{\text{tun-wide}}, \quad (11)$$

$$H_{\text{edge}} = \int_{-\infty}^{+\infty} dx \left(-i\psi_1^\dagger v \partial_x \psi_1 + i\psi_2^\dagger v \partial_x \psi_2 \right), \quad (12)$$

$$H_{\text{tun-wide}} = \zeta \int_0^W dx \left(\psi_1^\dagger(x) \psi_2(x) + \text{h.c.} \right). \quad (13)$$

Solving the scattering problem for H_{wqp} (see Appendix B for derivation), one finds the transmission func-

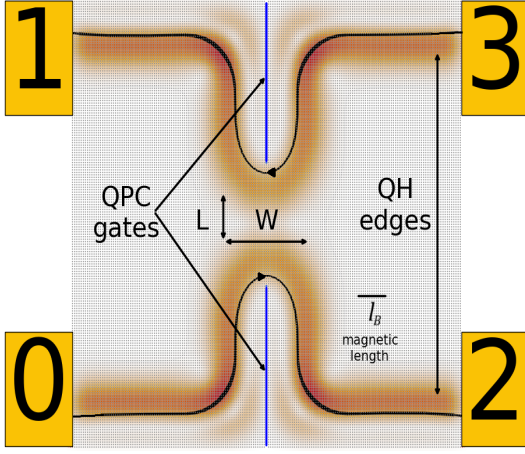


Figure 3. **Numerical simulation of a QPC geometry with narrow QPC-defining gates.** The figure presents the current density of QH edges in a sample that has four leads and a QPC defined by infinite potential on narrow gates (blue lines). The sample is modeled as 180x180 lattice, and the QPC-defining potential is applied to regions of 1-site width and 70-site length. The red density map represents the current density of two edge states. The edge states go around the gated regions smoothly, so that the tunneling would happen over a finite QPC width of a few magnetic lengths (W). This motivates our wide-QPC model shown in Fig. 4. The distance L between the edges in the QPC determines the size of the gapped system bulk between the edges. This motivated our long-QPC model shown in Fig. 6. The simulation has been performed using KWANT package [37].

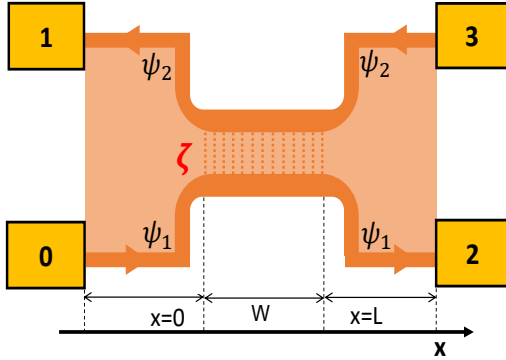


Figure 4. **Wide-QPC model.** Two chiral edge channels undergo tunneling over a finite region of width W .

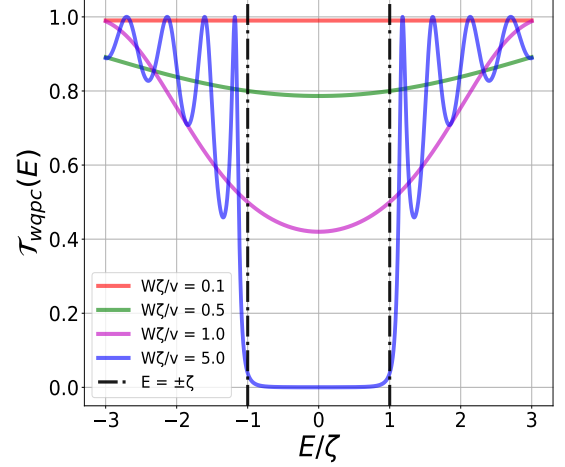


Figure 5. **The dependence of $\mathcal{T}_{\text{wqpc}}(E)$ on energy for various values of $\zeta W/v$.** The value of the dimensionless parameter $\zeta W/v$ determines $\mathcal{T}_{\text{wqpc}}(E=0)$. At $|E| \rightarrow \infty$, the transmission becomes perfect, $\mathcal{T}_{\text{wqpc}}(E) \rightarrow 1$. Oscillatory behavior for $|E| > \zeta$ strongly depends on $\zeta W/v$.

tion for wide-QPC model ($\mathcal{T}_{0 \rightarrow 2}^{\text{wqpc}}$) as:

$$\mathcal{T}_{\text{wqpc}}(E) = \mathcal{T}_{\text{wqpc}}^{0 \rightarrow 2} = \frac{1}{1 + \Xi(E, \zeta, W)}, \quad (14)$$

$$\text{where } \Xi(E, \zeta, W) = \frac{\sinh^2 \left(\frac{\zeta W}{v} \sqrt{1 - \left(\frac{E}{\zeta} \right)^2} \right)}{\left(1 - \left(\frac{E}{\zeta} \right)^2 \right)}$$

$$= \frac{\sin^2 \left(\frac{\zeta W}{v} \sqrt{\left(\frac{E}{\zeta} \right)^2 - 1} \right)}{\left(\left(\frac{E}{\zeta} \right)^2 - 1 \right)}.$$

Note that unlike in the case of point-QPC model, here the transmission depends on energy.

The typical scale for the energy is the tunneling amplitude ζ , whereas the overall behavior of the transmission is determined by the dimensionless parameter $\zeta W/v$. Indeed, at $\mathcal{T}_{\text{wqpc}}(E=0) = \left[1 + \sinh^2 \left(\frac{\zeta W}{v} \right) \right]^{-1}$. At large energies, the transmission is perfect: $\mathcal{T}_{\text{wqpc}}(|E| \gg \zeta) = 1$. At the characteristic scale, $\mathcal{T}_{\text{wqpc}}(|E| = \zeta) = \left[1 + \left(\frac{\zeta W}{v} \right)^2 \right]^{-1}$.

The behavior of $\mathcal{T}_{\text{wqpc}}(E)$ at various values of $\zeta W/v$ is shown in Fig. 5. Several aspects are worth noting. The strength of energy dependence of $\mathcal{T}_{\text{wqpc}}(E)$ varies with $\zeta W/v$ in a non-trivial way. In particular, for $|E| > \zeta$, $\mathcal{T}_{\text{wqpc}}(E)$ oscillates, cf. Eq. (14). The oscillation frequency, however, depends on $\zeta W/v$ and is only noticeable for large $\zeta W/v$ in Fig. 5.

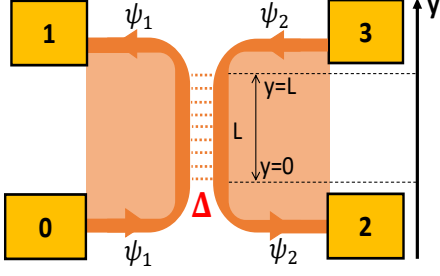


Figure 6. **Long QPC model.** In order to model the tunneling barrier created by the bulk gap inside the QPC (cf. Fig. 1), we model the bulk in the spirit of the wire construction. The region of strong electron tunneling (amplitude Δ) across the region devoid of electrons is topologically equivalent to the bulk of the quantum Hall sample.

C. Long model

In the models considered above (point QPC and wide QPC), the tunneling amplitude between the edges was treated as a phenomenological parameter. However, the intuition based on quantum mechanics tells that the tunneling arises from a barrier that makes it energetically costly for quasiparticles to be between the two edges in the QPC. This barrier may govern the energy dependence of the tunneling amplitude, and thus of the transmission probability $\mathcal{T}(E)$.

In order to model this dependence, we model the QH bulk region of size L inside the QPC, cf. Fig. 3, in the spirit of the wire construction [32]. In its general form, the wire construction models the QH bulk as a 1D array of one-dimensional wires with appropriate tunneling processes between them. Here we use a minimalistic model, framing the QPC as two edges, between which electrons tunnel across a depleted region, cf. Fig. 6. The tunneling amplitude Δ corresponds to the bulk gap, cf. Appendix B 1, and the length of the tunneling region L corresponds to the distance between the edges on the different sides of the QPC — these parameters have notably been absent from the point- and wide-QPC models.¹

The Hamiltonian for the long-QPC model is

$$H_{\text{lqpc}} = H_{\text{edge}} + H_{\text{tun-long}}, \quad (15)$$

$$H_{\text{edge}} = \int_{-\infty}^{+\infty} dy \left(-i\psi_1^\dagger v \partial_y \psi_1 + i\psi_2^\dagger v \partial_y \psi_2 \right), \quad (16)$$

$$H_{\text{tun-long}} = \Delta \int_0^L dy \left(\psi_1^\dagger(y) \psi_2(y) + \text{h.c.} \right). \quad (17)$$

¹ While here we consider the example of integer QH effect, the generalization of this model for the fractional QH effect would reflect the famous duality of weak quasiparticle tunneling and strong electron tunneling [19, 24, 38, 39].

Note that the Hamiltonian for the long-QPC model is formally identical to that of the wide-QPC model, Eqs. (11–13). The two Hamiltonians differ by the substitutions $x \rightarrow y$, $\zeta \rightarrow \Delta$, and $W \rightarrow L$, which reflects the conceptual difference between the models. Most importantly, the models differ by the connection of ψ_1 and ψ_2 to different Ohmic contacts, cf. Figs. 4 and 6.

This enables us to reuse the solution of the wide-QPC model (14), while accounting for these distinctions:

$$\begin{aligned} \mathcal{T}_{\text{lqpc}}(E) &= \mathcal{T}_{\text{lqpc}}^{0 \rightarrow 2} = 1 - \mathcal{T}_{\text{lqpc}}^{0 \rightarrow 1} \\ &= 1 - \mathcal{T}_{\text{wqpc}}^{0 \rightarrow 2} \Big|_{\substack{\zeta \rightarrow \Delta \\ W \rightarrow L}} = \frac{\Xi(E, \Delta, L)}{1 + \Xi(E, \Delta, L)}, \end{aligned} \quad (18)$$

$$\begin{aligned} \text{where } \Xi(E, \Delta, L) &= \frac{\sinh^2 \left(\frac{L\Delta}{v} \sqrt{1 - \left(\frac{E}{\Delta} \right)^2} \right)}{\left(1 - \left(\frac{E}{\Delta} \right)^2 \right)} \\ &= \frac{\sin^2 \left(\frac{L\Delta}{v} \sqrt{\left(\frac{E}{\Delta} \right)^2 - 1} \right)}{\left(\left(\frac{E}{\Delta} \right)^2 - 1 \right)}. \end{aligned}$$

Similarly to the wide-QPC model and in contrast to the standard point-QPC model, the transmission function in the long-QPC model explicitly depends on energy. However, the nature of the dependence is drastically different as compared to the wide-QPC model.

Indeed, the transmission is *maximum* at $E = 0$ and goes to zero at large energies, $\mathcal{T}_{\text{lqpc}}(|E| \gg \Delta) = 0$, cf. Fig. 7. This is natural as for $|E| \ll \Delta$ the quasiparticles are unlikely to tunnel across the QPC, and are likely to be transmitted. Conversely, for $|E| \gg \Delta$, the bulk gap does not present a significant obstacle for quasiparticles to travel to a different edge. Of course, our crude model does not capture all the important aspects of the QH bulk, notably its disordered nature. However, our model does capture the concept of the tunneling barrier.

The value of transmission $\mathcal{T}_{\text{lqpc}}(E = 0) = [1 + \sinh^{-2}(\frac{L\Delta}{v})]^{-1}$ is controlled by the dimensionless parameter $L\Delta/v$ that captures the barrier height Δ and length L . We do not expect our model to be valid beyond $|E| = \Delta$, where proper bulk modeling needs to be performed. At this energy scale, $\mathcal{T}_{\text{lqpc}}(|E| = \Delta) = [1 + (\frac{L\Delta}{v})^{-2}]^{-1}$.

IV. POINT-QPC LIMIT

The models introduced in the previous section can be viewed as generalizations of the point-QPC model, incorporating aspects of realistic QPC setups. The wide- and long-QPC models allow a parameter regime ($L \rightarrow 0$) that reduces them back to the point-QPC geometry. It is natural to expect the predictions for $\mathcal{T}(E)$ to reduce

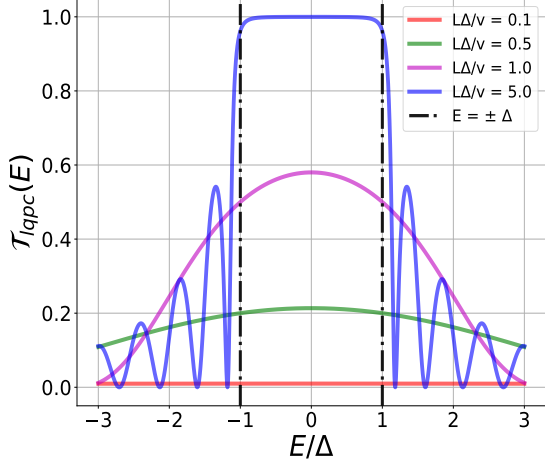


Figure 7. **The dependence of $\mathcal{T}_{\text{lqpc}}(E)$ on energy for various values of $L\Delta/v$.** The dimensionless parameter $L\Delta/v$ is associated to the “area of the tunneling barrier”, $L\Delta$. Its value determines $\mathcal{T}_{\text{lqpc}}(E=0)$. At $|E| \rightarrow \infty$, the transmission decays to zero, $\mathcal{T}_{\text{lqpc}}(E) \rightarrow 0$. The vertical black lines $E = \pm\Delta$, marks the magnitude of the bulk gap Δ ; we do not expect our model to be valid beyond this energy scale.

to those of the point-QPC model in this limit. Below we show that this is not the case, which points at the singularity of the point-QPC model.

Consider the wide-QPC model. Taking the limit $W \rightarrow 0$, $\zeta \rightarrow \infty$ such that $\zeta W = \text{const}$, the Hamiltonian of the wide-QPC model (11–13) reduces to that of the point-QPC model (7–9) with $\eta_{\text{wqpc}} = \zeta W$. Taking the limit for the transmission function (14) yields

$$\mathcal{T}_{\text{wqpc}}(E) = \mathcal{T}_{\text{wqpc}}^{(\text{point limit})} = \frac{1}{1 + \sinh^2\left(\frac{\eta_{\text{wqpc}}}{v}\right)}. \quad (19)$$

Compare this to $\mathcal{T}_{\text{pqc}}(E)$ in Eq. (10). Both expressions predict no energy dependence of the transmission function and both predict $\mathcal{T}(E) \approx 1 - \eta^2/v^2$ for $|\eta| \ll v$. However, for η comparable or larger than v , the models yield drastically different predictions, despite having the identical Hamiltonian in this limit. In particular, the point-QPC model predicts $\mathcal{T}_{\text{pqc}}(E) = 0$ at $\eta = 2v$ and $\mathcal{T}_{\text{pqc}}(E) = 1$ at $\eta \rightarrow \infty$. At the same time, $\mathcal{T}_{\text{wqpc}}^{(\text{point limit})}$ is monotonous with respect to η_{wqpc} and vanishes for $\eta_{\text{wqpc}} \rightarrow \infty$.

The long-QPC model also features a point limit $L \rightarrow 0$, $\Delta \rightarrow \infty$ such that $L\Delta = \text{const}$. In this limit, its Hamiltonian (15–17) reduces to that of the point-QPC model (7–9) with $\eta_{\text{long}} = L\Delta$. However, the roles of the contacts 1 and 2 are interchanged compared to the wide- and point-QPC models, cf. Figs. 2, 4, 6. Taking the limit for the transmission function, one gets

$$\mathcal{T}_{\text{lqpc}}(E) = \mathcal{T}_{\text{lqpc}}^{(\text{point limit})} = \frac{\sinh^2\left(\frac{\eta_{\text{lqpc}}}{v}\right)}{1 + \sinh^2\left(\frac{\eta_{\text{lqpc}}}{v}\right)}. \quad (20)$$

Again, this predicts an energy-independent transmission function in the point limit, yet does not match $\mathcal{T}_{\text{pqc}}^{0 \rightarrow 1} = 1 - \mathcal{T}_{\text{pqc}}^{0 \rightarrow 2}$ in its dependence on η , see Eq. (10).

This shows that the point-QPC model (7–9) is ill-defined: depending on the regularization of the point tunneling, the model produces different results. This has, in fact, been highlighted before in Ref. [36].

These results are in stark contrast to the case of point barrier in the conventional quantum mechanics for $p^2/(2m)$ dispersion relation, where the transmission across the delta-barrier is reproduced by taking the point limit of a rectangular potential, see Appendix C. It may be interesting to investigate in the future whether incorporating the curvature of the dispersion relation into the model (i.e., the terms $\sim \psi_i^\dagger \partial_x^2 \psi_i$) would eliminate the above singularity of the point-QPC model.

V. MODEL COMPARISON WITH REALISTIC PARAMETERS

Above, we have defined three distinct QPC models and derived their predictions for the transmission function $\mathcal{T}(E)$. In this section, we compare these models using experimentally realistic parameters. In Sec. VA, we compare their predictions for the transmission functions. In Sec. VB, we show how these predictions translate to experimentally observable quantities.

A. Model comparison with experimentally realistic parameters

Above, we have derived the energy dependence of the transmission function $\mathcal{T}(E)$ as predicted by the point-QPC, wide-QPC, and long-QPC models. These predictions exhibit qualitatively different behaviors: for the wide-QPC model, the minimum value of $\mathcal{T}(E)$ is achieved at $E = 0$ (Fig 5) whereas in long-QPC model $E = 0$ corresponds to the maximum of $\mathcal{T}(E)$ (Fig 7). Therefore, different aspects of realistic QPC geometry predict different energy dependences of $\mathcal{T}(E)$. However, what is the significance of those dependences in realistic systems? We investigate this question below.

We begin by estimating the experimental parameters appropriate for typical QPC setups. Consider a GaAs-based quantum Hall sample with an electron density $n_s = 1 \times 10^{15} \text{ m}^{-2}$. Given the effective mass $m^* = 0.067m_e$ (with m_e is the bare electron mass), the filling factor $\nu = 1$ is achieved for the magnetic field $B = 4.14 \text{ T}$, which further sets the magnetic length $l_B = 12.6 \text{ nm}$ and the cyclotron energy $E_c = \hbar\omega_c = 7.17 \text{ meV}$.

The edge state velocity may vary depending on the sample: values of the orders $v = 10^4$ – 10^6 m/s have been reported depending on whether the quantum Hall edge is defined by a gate or by the boundary of the sample [12, 40–46]. Given that the velocity of interest for us is the velocity inside the QPC that is typically gate-defined,

we take the value on the lower end of the range, $v = 2 \cdot 10^4$ m/s [44].

Given the system parameters, we can now estimate the relevant parameters of our QPC models. For the wide-QPC model, the parameters are the tunneling amplitude, ζ , and the width of the tunneling region, W . The QPC width can hardly be smaller than a few magnetic lengths. Indeed, Fig. 3 shows that even for infinitely-small QPC-defining gate, the tunneling region has double the width of the edge wave function. With the edge wave function having the width $l_B\sqrt{2}$ [47, Section 9.5.4], we take $W = 2\sqrt{2}l_B$. The tunneling amplitude ζ is then determined by the transmission value at zero energy, $\mathcal{T}_0 = \mathcal{T}(E=0)$, from Eq. (14):

$$\zeta = \frac{\hbar v}{W} \sinh^{-1} \left(\sqrt{\frac{1 - \mathcal{T}_0}{\mathcal{T}_0}} \right), \quad (21)$$

where we have explicitly restored \hbar . This gives the values of $\zeta = 0.45, 0.22$, and 0.08 meV for $\mathcal{T}_0 = 0.1, \mathcal{T}_0 = 0.5$, and $\mathcal{T}_0 = 0.9$ respectively.

For the long-QPC model, the parameters are the tunneling amplitude, Δ , and the QPC length, L . The value of 2Δ is natural to identify with the bulk gap of the quantum Hall sample, cf. Appendix B 1. Therefore, $\Delta = E_c/2 = 3.58$ meV. The length of the QPC is then determined by the zero-energy transmission \mathcal{T}_0 through Eq. (18):

$$L = \frac{\hbar v}{\Delta} \sinh^{-1} \left(\sqrt{\frac{\mathcal{T}_0}{1 - \mathcal{T}_0}} \right). \quad (22)$$

This yields the values of $L = 1.2, 3.2$, and 6.7 nm for $\mathcal{T}_0 = 0.1, \mathcal{T}_0 = 0.5$, and $\mathcal{T}_0 = 0.9$ respectively.

Given the parameters estimated above, the dependences $\mathcal{T}(E)$ are shown in Fig. 8(a). The range of energies on the horizontal axis is chosen to correspond to the typical bias voltages (100–300 μ V) used in experiments. One sees that the long-QPC does not predict any noticeable deviation of $\mathcal{T}(E)$ from constant. This is due to the energies of interest being much smaller than the bulk gap $2\Delta = E_c$. The wide-QPC model, though, produces noticeable deviations. This shows that the QPC width is an important effect even for the narrowest QPCs possible.

We investigate the variation of $\mathcal{T}(E)$ at energies beyond the typical voltage range in experiments in Fig. 8(b). One sees a much stronger variation of transmission. Here, the long-QPC model predicts a noticeable deviation from the point-QPC model. The wide-QPC model exhibits an extremely strong variation of transmission, with saturation at $\mathcal{T}(E) = 1$ and oscillations indicative of resonances in the QPC region.

These $\mathcal{T}(E)$ dependences translate into experimentally measurable quantities: the QPC current, the current noise, and the Fano factor. We investigate predictions for those quantities in Sec. V B.

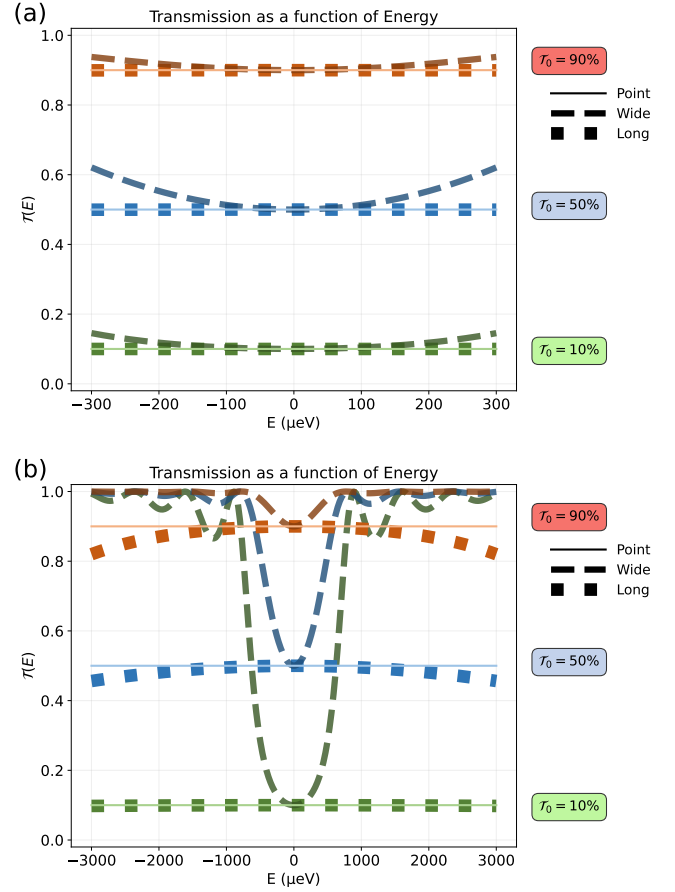


Figure 8. **Transmission $\mathcal{T}(E)$ for various models for experimentally realistic parameters.** (a) Comparison of the dependence of QPC transmission on energy that point-, wide-, and long-QPC models predict for realistic experimental parameters. The effects of the long-QPC model are negligible in the experimentally relevant regime. Whereas the width of the QPC does have a noticeable effect. These predictions are obtained using edge velocity $v = 2 \cdot 10^4$ m/s. The role of velocity is further discussed in Appendix D. (b) Comparison of QPC energy-dependent transmission for the same set of models for energy scales beyond the typical experimental range. The effects of the long-QPC model become noticeable as the scale becomes comparable with the cyclotron gap $E_c = \hbar\omega_c = 7.17$ meV. The wide-QPC model predicts an even stronger dependence with transmission saturating at 1 (up to small oscillations) at large energies.

B. Transport predictions

In the previous section, we analyzed the transmission functions associated with three distinct models with realistic experimental parameters in the conventional experimental regime. In this section, we investigate the predictions for transport quantities — specifically, the differential conductance, current, noise, and the Fano factor — within the point-, wide-, and long-QPC models. We use the same parameters as above for the three models,

and take the chemical potential values for the contacts as $\mu_L = -\mu_R = eV/2$, where V is the bias voltage. We take the system temperature to be $T = 10$ mK (experiments typically use $T = 10$ – 40 mK).

Using Eqs. (3–4), the current $I_2(V)$ and noise S_{22} for each model are obtained directly from the corresponding transmission function $\mathcal{T}(E)$. The differential conductance is defined as

$$g = dI_2/dV. \quad (23)$$

We define the excess noise as the component of the noise beyond the Johnson–Nyquist contribution:

$$S_E = S_{22}(V) - S_{22}(V=0).$$

Further, we consider a dimensionless parameter called the Fano factor. We define it as,

$$F = \frac{S_E(V)}{2e\left(\frac{e^2}{h}V\right)\bar{\mathcal{T}}(V)(1-\bar{\mathcal{T}}(V))}; \quad \bar{\mathcal{T}}(V) = \frac{I_2}{I_0} \quad (24)$$

where $\bar{\mathcal{T}}(V)$ is average transmission at a given voltage, defined as ratio of the transmitted current I_2 to the injected current ($I_0 = \frac{e^2}{h}V$). Note that this definition is slightly different from the standard Fano factor definition due to inclusion of $(1 - \bar{\mathcal{T}}(V))$ in the denominator. This modification allows one to treat $\bar{\mathcal{T}} \approx 0$ and $\bar{\mathcal{T}} \approx 1$ on an equal footing and is often employed in experimental papers.

The results for $|V| \leq 300$ μ V (which is the typical voltage range in modern experiments) are presented in Fig. 9. Similarly to the behavior of transmission $\mathcal{T}(E)$ in Fig. 8(a), the long-QPC model is indistinguishable from the point-QPC model in this voltage range. The wide-QPC model does exhibit noticeable yet small deviations from the point-QPC predictions. These deviations are can be seen in the behavior of the differential conductance g and the excess noise S_E , yet are completely unnoticeable in the behaviors of the total current I_2 and the Fano factor F .

Extending the energy range in the spirit of Fig. 8(b), we consider also the voltages up to 3000 μ V. The transport observables in this voltage range are presented in Fig. 10. Here the long-QPC model exhibits small deviations from the point-QPC model for large V (noticeable in g_2 and, for large \mathcal{T}_0 , in S_E , but not in I_2 or F). The deviations predicted by the wide-QPC model become significant for all observables in this voltage range (for which $e|V|$ is still significantly smaller than the bulk gap of $E_c = 7.17$ meV).

VI. CONCLUSION

In this work, we have considered extension of the standard point-QPC model to account for realistic QPC geometry. Specifically, we have introduced a model that

accounts for the QPC width (wide-QPC model), and another model that accounts for a finite distance between the edges across the QPC (“length of the tunneling barrier”, long-QPC model). We have shown that, in contrast to the point-QPC model, both models predict energy dependence of the transmission function $\mathcal{T}(E)$.

We have investigated this prediction for realistic parameters in the regime of integer ($\nu = 1$) quantum Hall effect. We have shown that the effect of the QPC width, W , on the behavior of the transmission function is much more significant than that of the “QPC length”, L . For standard experimental parameters and typical ranges investigated, the wide-QPC model does predict a noticeable energy dependence of $\mathcal{T}(E)$ (cf. Fig. 8), which, however, hardly translates into noticeable effects in transport experiments (cf. Fig. 9). This shows that the energy dependences of $\mathcal{T}(E)$ stemming from QPC geometries are unlikely to explain any deviations from point-QPC predictions, at least in the integer QH regime.

Extending the range of bias voltages beyond the ones used in modern experiments, one can see clear effects of the QPC width in transport observables (cf. Fig. 10), even if the width is of the order of the magnetic length l_B . This extended bias voltage range still corresponds to energies significantly below the bulk gap. Therefore, performing experiments within the extended range and comparing their results to predictions of edge models would be meaningful.

Finally, we note that our models do not account for the energy dependence of the edge velocity. Introducing this aspect to the models in the future has twofold importance. It may be necessary for modeling realistic experiments. And from a purely theoretical point of view, it could lift the singular behavior of the point-QPC model (see the discussion in Sec. IV).

ACKNOWLEDGMENTS

We acknowledge funding from the European Union’s Horizon 2020 research and innovation program under Grant agreement No. 862683 (UltraFast Nano), from the French ANR DADDI and T-KONDO and from State aid managed by the Agence Nationale de la Recherche under the France 2030 program, reference ANR-22-PETQ-0012 (EQUBITFLY).

This paper was prepared with the help of **LyX** editor.

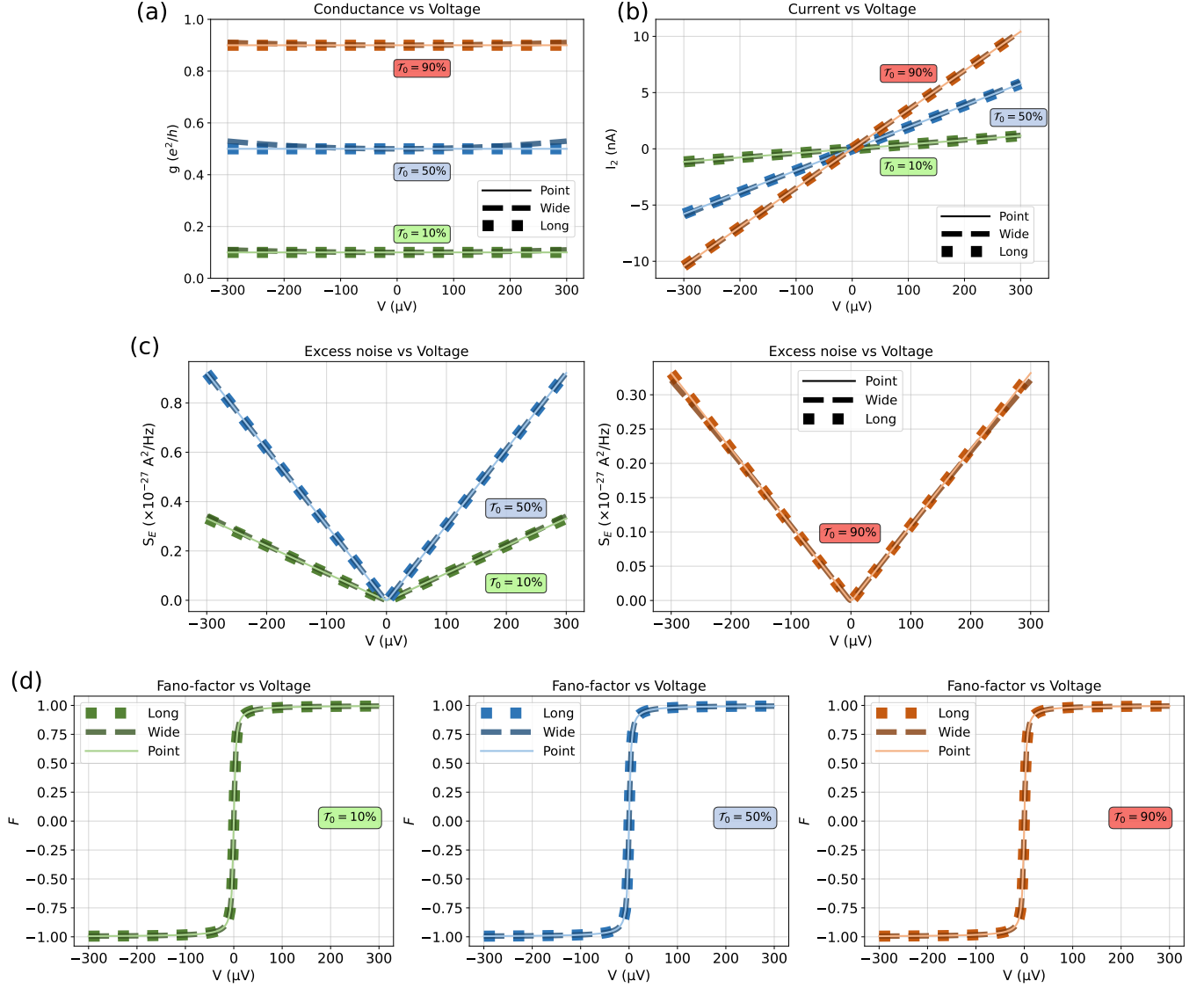


Figure 9. **Transport observables for point-, wide-, and long-QPC models for experimentally realistic parameters as a function of the bias voltage V .** (a) Differential conductance g . The wide-QPC model predicts a slightly higher g at large $|V|$, as compared to the point-QPC model. (b) Current I_2 . No deviation between the models is noticeable. (c) Excess noise S_E . At low and high transmissions T_0 , the noise is slightly increased in the wide-QPC model at large $|V|$. (d) Fano-factor F . No deviation between the models is noticeable.

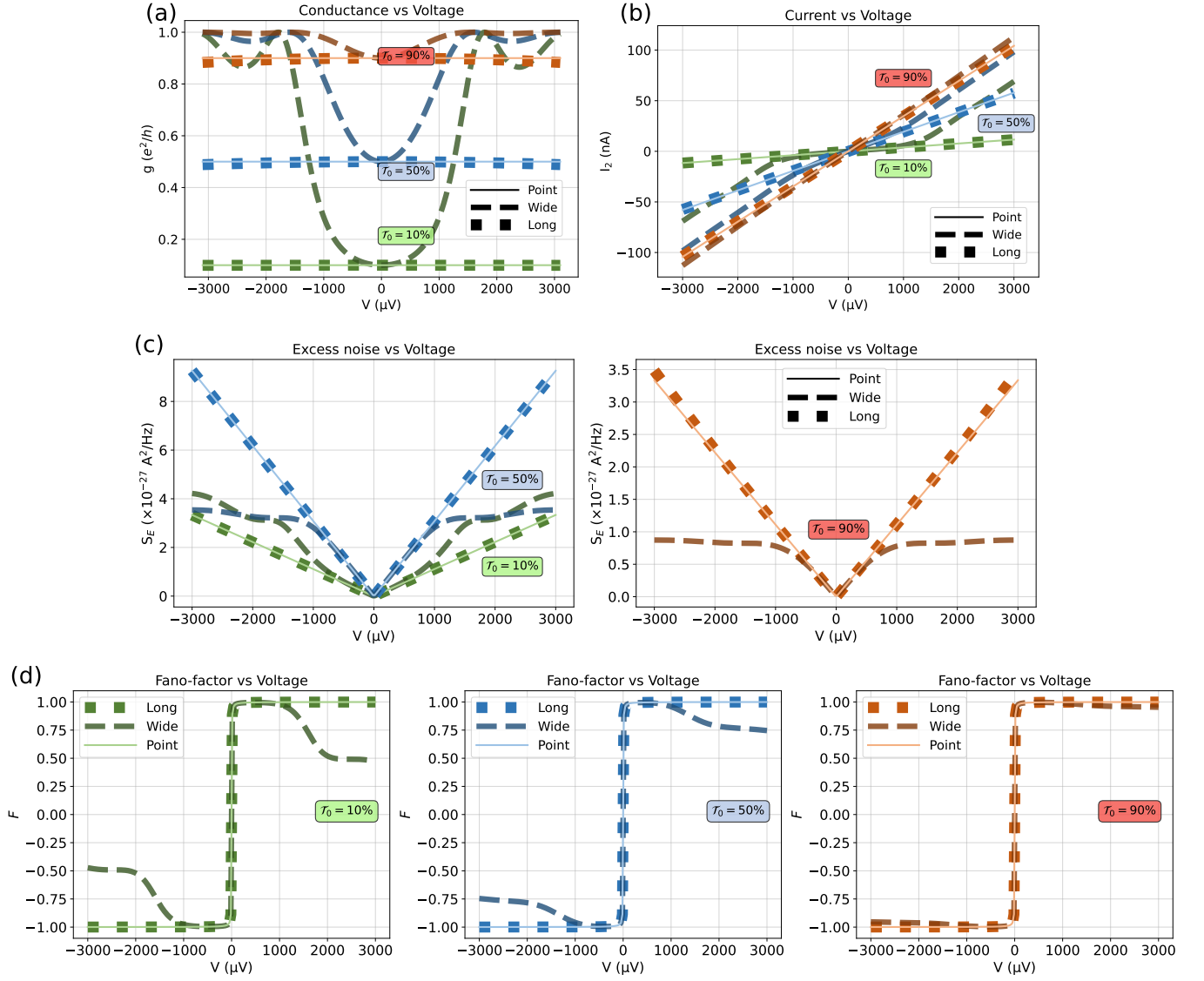


Figure 10. **Transport observables for different QPC models for a voltage range larger than typically investigated, yet experimentally reasonable.** (a) Differential conductance g . (b) Current I_2 . (c) Excess noise S_E . (d) Fano-factor F . The long-QPC model exhibits small deviations from the point-QPC for some observables. The deviations predicted by the wide-QPC model are significant for all observables.

Appendix A: Derivation of the transmission function for point QPC

In this Appendix, we provide the derivation of the point-QPC transmission function (10). For brevity of notation, we put $\hbar = 1$ in this section.

We start with the Hamiltonian (7–9). This yields the following equations of motion for the fields:

$$\begin{aligned}\partial_t \psi_1(x) &= i[H, \psi_1(x)] \\ &= -v\partial_x \psi_1(x) - i\eta\psi_2(x)\delta(x),\end{aligned}\quad (\text{A1})$$

$$\begin{aligned}\partial_t \psi_2(x) &= i[H, \psi_2(x)] \\ &= v\partial_x \psi_2(x) - i\eta\psi_1(x)\delta(x).\end{aligned}\quad (\text{A2})$$

Looking for solutions in the form

$$\psi_1(x) = \sum_n \hat{a}_n \phi_{n,1}(x) e^{-iE_n t}, \quad (\text{A3})$$

$$\psi_2(x) = \sum_n \hat{a}_n \phi_{n,2}(x) e^{-iE_n t}, \quad (\text{A4})$$

where \hat{a}_n are the Fermionic annihilation operators, we arrive at equations for the wave functions of the system's eigenmodes:

$$\begin{aligned}E_n \phi_{n,1}(x) \\ = -iv\partial_x \phi_{n,1}(x) + \eta\phi_{n,2}(x=0)\delta(x),\end{aligned}\quad (\text{A5})$$

$$\begin{aligned}E_n \phi_{n,2}(x) \\ = iv\partial_x \phi_{n,2}(x) + \eta\phi_{n,1}(x=0)\delta(x).\end{aligned}\quad (\text{A6})$$

Integrating these equations around $x = 0$, one finds the boundary condition enforced by the delta function:

$$\phi_1(0^+) - \phi_1(0^-) = -\frac{i\eta}{v}\phi_2(x=0), \quad (\text{A7})$$

$$\phi_2(0^+) - \phi_2(0^-) = \frac{i\eta}{v}\phi_1(x=0). \quad (\text{A8})$$

Equations (A5–A6) away from $x = 0$ are solved by

$$\phi_1(x) = \begin{cases} He^{(i\frac{Ex}{v})} & \text{for } x > 0 \\ Ae^{(i\frac{Ex}{v})} & \text{for } x < 0 \end{cases}, \quad (\text{A9})$$

$$\phi_2(x) = \begin{cases} Ge^{(-i\frac{Ex}{v})} & \text{for } x > 0 \\ Be^{(-i\frac{Ex}{v})} & \text{for } x < 0 \end{cases}. \quad (\text{A10})$$

The boundary conditions (A7–A8) then yield

$$H - A = -\frac{i\eta}{v} \left(\frac{B + G}{2} \right), \quad (\text{A11})$$

$$G - B = \frac{i\eta}{v} \left(\frac{A + H}{2} \right), \quad (\text{A12})$$

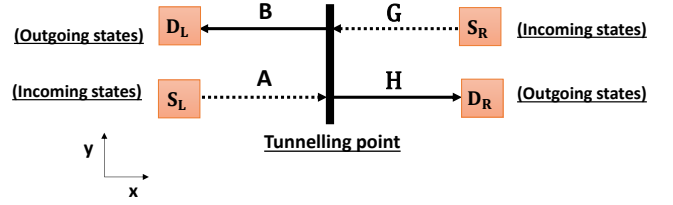


Figure 11. **Scattering point of view on the QPC physics.** The sketch represents the QPC setup of Fig. 1 with explicit connection to the wave function in Eqs. (A9–A10). S_L and S_R are the sources on the left and the right side of the QPC. The dotted lines represent the incoming edge states while the dark lines are the outgoing edge states.

leading to the solution

$$H = -\frac{iG}{\left(\frac{v}{\eta} + \frac{\eta}{4v}\right)} + \frac{A\left(\frac{v}{\eta} - \frac{\eta}{4v}\right)}{\left(\frac{v}{\eta} + \frac{\eta}{4v}\right)}, \quad (\text{A13})$$

$$B = -\frac{iA}{\left(\frac{v}{\eta} + \frac{\eta}{4v}\right)} + \frac{G\left(\frac{v}{\eta} - \frac{\eta}{4v}\right)}{\left(\frac{v}{\eta} + \frac{\eta}{4v}\right)}. \quad (\text{A14})$$

Identifying A and G with the amplitudes of the incoming states, and H and B with those of outgoing states (cf. Fig. 11), one can infer the transmission and reflection amplitudes. Setting $G = 0$ (S_R is off), one finds

$$t_L = \frac{H}{A} = \frac{\left(\frac{v}{\eta} - \frac{\eta}{4v}\right)}{\left(\frac{v}{\eta} + \frac{\eta}{4v}\right)} = \frac{\left(1 - \frac{\eta^2}{4v^2}\right)}{\left(1 + \frac{\eta^2}{4v^2}\right)}, \quad (\text{A15})$$

$$r_L = \frac{B}{A} = \frac{-i}{\left(\frac{v}{\eta} + \frac{\eta}{4v}\right)}. \quad (\text{A16})$$

Similarly, setting $A = 0$ (S_L is off) leads to

$$t_R = \frac{B}{G} = \frac{\left(\frac{v}{\eta} - \frac{\eta}{4v}\right)}{\left(\frac{v}{\eta} + \frac{\eta}{4v}\right)} = \frac{\left(1 - \frac{\eta^2}{4v^2}\right)}{\left(1 + \frac{\eta^2}{4v^2}\right)}, \quad (\text{A17})$$

$$r_R = \frac{H}{G} = \frac{-i}{\left(\frac{v}{\eta} + \frac{\eta}{4v}\right)}. \quad (\text{A18})$$

One readily checks the unitarity of the scattering matrix \mathcal{S} (1): $\mathcal{S}\mathcal{S}^\dagger = \mathcal{S}^\dagger\mathcal{S} = I$, where I is the identity matrix. The transmission function $\mathcal{T}_{\text{QPC}}(E) = |t_L|^2$ is then given by Eq. (10).

Appendix B: Derivation of the transmission function for wide QPC

Here we derive the transmission function for the wide-QPC model (Fig. 4), which is defined through Eqs. (11–13). Before providing the derivation in Sec. B2, we

discuss the properties of the extended region that features tunneling processes. For brevity of notation, we put $\hbar = 1$ in this section.

1. The properties of the region with tunneling

In order to understand the properties of the extended region that features tunneling processes, it is instructive to consider Hamiltonian

$$H = \int_{-\infty}^{+\infty} dx \left(-i\psi_1^\dagger v \partial_x \psi_1 + i\psi_2^\dagger v \partial_x \psi_2 \right) + \zeta \int_{-\infty}^{+\infty} dx \left(\psi_1^\dagger(x) \psi_2(x) + \psi_2^\dagger(x) \psi_1(x) \right). \quad (\text{B1})$$

Compared to Eqs. (11–13), we have taken the tunneling region to be infinite.

Since the system is translationally invariant, one can represent the solution to the equations of motion

$$\partial_t \psi_1(x) = i[H, \psi_1(x)] = -v \partial_x \psi_1(x) - i\zeta \psi_2(x), \quad (\text{B2})$$

$$\partial_t \psi_2(x) = i[H, \psi_2(x)] = v \partial_x \psi_2(x) - i\zeta \psi_1(x), \quad (\text{B3})$$

in the form

$$\psi_1(x) = \sum_k \hat{a}_k A_1 e^{ikx - iE_k t}, \quad (\text{B4})$$

$$\psi_2(x) = \sum_k \hat{a}_k A_2 e^{ikx - iE_k t}, \quad (\text{B5})$$

where \hat{a}_k are the fermionic annihilation operators. The equations of motion then yield

$$\begin{pmatrix} vk & \zeta \\ \zeta & -vk \end{pmatrix} \begin{pmatrix} A_1 \\ A_2 \end{pmatrix} = E_k \begin{pmatrix} A_1 \\ A_2 \end{pmatrix}. \quad (\text{B6})$$

The solution of this equation for eigenmodes leads to the spectrum $E_k = \pm \sqrt{(vk)^2 + \zeta^2}$. We thus see that the region with tunneling features an energy gap of the size 2ζ (cf. Fig. 12), which serves as an extended tunneling barrier in the wide-QPC model.

Note that the long-QPC model, cf. Fig. 6 and Eqs. (15–17), features the same Hamiltonian as the wide-QPC one — up to renaming $x \rightarrow y$, $\zeta \rightarrow \Delta$, and $W \rightarrow L$. The interpretation of the long-QPC model is very different, though. The tunneling region in the long-QPC model is designed to mimic the bulk of the system. Therefore, 2Δ is natural to identify with the bulk gap. This was used to estimate the realistic model parameters in Sec. V.

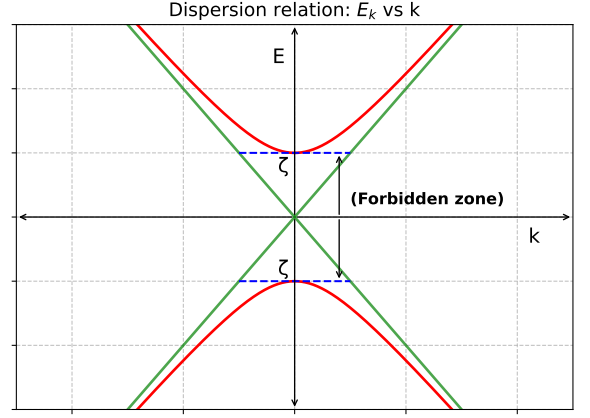


Figure 12. Dispersion relation of the fermions in an infinite tunneling region, cf. Eq. (B1). The dispersion relation of edges without tunneling $E_k = \pm vk$ is shown in green. In the presence of tunneling, $E_k = \pm \sqrt{(vk)^2 + \zeta^2}$ (red), exhibiting a forbidden zone of size 2ζ .

2. The transmission function

Now that we understand the effect of an extended region with tunneling, we are in position to derive the transmission function for the wide-QPC model. Starting from Eqs. (11–13), one obtains the equations of motion for the right-moving edge:

$$\partial_t \psi_1(x) = i[H, \psi_1(x)] \quad (\text{B7})$$

$$= \begin{cases} -v \partial_x \psi_1(x), & x \notin (0, W), \\ -v \partial_x \psi_1(x) - i\zeta \psi_2(x), & x \in (0, W). \end{cases} \quad (\text{B8})$$

Similarly, for the left-moving edge:

$$\partial_t \psi_2(x) = i[H, \psi_2(x)] \quad (\text{B9})$$

$$= \begin{cases} v \partial_x \psi_2(x), & x \notin (0, W), \\ v \partial_x \psi_2(x) - i\zeta \psi_1(x), & x \in (0, W). \end{cases} \quad (\text{B10})$$

Looking for the solution in the form (A3–A4), we find

$$\frac{d}{dx} \begin{pmatrix} \phi_1(x) \\ \phi_2(x) \end{pmatrix} = \frac{i}{v} \begin{pmatrix} E & 0 \\ 0 & -E \end{pmatrix} \begin{pmatrix} \phi_1(x) \\ \phi_2(x) \end{pmatrix} \quad \text{for } x \in (0, W), \quad (\text{B11})$$

and

$$\frac{d}{dx} \begin{pmatrix} \phi_1(x) \\ \phi_2(x) \end{pmatrix} = \frac{i}{v} \begin{pmatrix} E & -\zeta \\ \zeta & -E \end{pmatrix} \begin{pmatrix} \phi_1(x) \\ \phi_2(x) \end{pmatrix} \quad \text{for } x \notin (0, W). \quad (\text{B12})$$

The wave function $\Phi(x) = (\phi_1(x), \phi_2(x))^T$ can thus be expressed in three regions:

$$\Phi(x) = \begin{cases} \Phi_{\text{I}} = \begin{pmatrix} Ae^{-iEx/v} \\ Be^{iEx/v} \end{pmatrix} = \begin{pmatrix} Ae^{-ikx} \\ Be^{ikx} \end{pmatrix}, & x < 0, \\ \Phi_{\text{II}} = \frac{C}{\sqrt{2E(E+i\kappa v)}} \begin{pmatrix} E+i\kappa v \\ \zeta \end{pmatrix} e^{-\kappa x} + \frac{D}{\sqrt{2E(E+i\kappa v)}} \begin{pmatrix} \zeta \\ E+i\kappa v \end{pmatrix} e^{\kappa x}, & 0 < x < W, \\ \Phi_{\text{III}} = \begin{pmatrix} He^{-iEx/v} \\ Ge^{iEx/v} \end{pmatrix} = \begin{pmatrix} He^{-ikx} \\ Ge^{ikx} \end{pmatrix}, & x > W. \end{cases} \quad (\text{B13})$$

Here $k = E/v$ and $\kappa = \sqrt{\zeta^2 - E^2}/v$.

The boundary conditions at $x = 0$ and $x = W$, enable expressing A , C , D , and G in terms of C and D .

$$\Phi_{\text{I}}(x=0) = \Phi_{\text{II}}(x=0) \quad (\text{B14})$$

$$\Rightarrow \begin{pmatrix} A \\ B \end{pmatrix} = \frac{C}{\sqrt{2E(E+i\kappa v)}} \begin{pmatrix} E+i\kappa v \\ \zeta \end{pmatrix} + \frac{D}{\sqrt{2E(E+i\kappa v)}} \begin{pmatrix} \zeta \\ E+i\kappa v \end{pmatrix}, \quad (\text{B15})$$

$$\Phi_{\text{II}}(x=W) = \Phi_{\text{III}}(x=W) \quad (\text{B16})$$

$$\Rightarrow \frac{C}{\sqrt{2E(E+i\kappa v)}} \begin{pmatrix} E+i\kappa v \\ \zeta \end{pmatrix} e^{-\kappa W} + \frac{D}{\sqrt{2E(E+i\kappa v)}} \begin{pmatrix} \zeta \\ E+i\kappa v \end{pmatrix} e^{\kappa W} = \begin{pmatrix} He^{-ikW} \\ Ge^{ikW} \end{pmatrix}. \quad (\text{B17})$$

Denoting

$$\alpha = E+i\kappa v, \beta = \zeta, \gamma = \sqrt{2E(E+i\kappa v)}, \quad (\text{B18})$$

and $e^{\pm\kappa W} = \cosh(\kappa W) \pm \sinh(\kappa W)$,

one can write

$$\gamma A = \alpha C + \beta D, \quad \gamma B = \alpha D + \beta C, \quad (\text{B19})$$

$$\gamma H = e^{ikW} [\alpha C e^{-\kappa W} + \beta D e^{\kappa W}], \quad \gamma G = e^{-ikW} [\beta C e^{-\kappa W} + \alpha D e^{\kappa W}]. \quad (\text{B20})$$

Conversely,

$$C = \frac{\gamma(\alpha A - \beta B)}{(\alpha^2 - \beta^2)}, \quad D = \frac{\gamma(\alpha B - \beta A)}{(\alpha^2 - \beta^2)}, \quad (\text{B21})$$

which enables one to find H and G in terms of A and B :

$$H = e^{ikW} \left[\left(\cosh(\kappa W) + \left(\frac{iE}{\kappa v} \right) \sinh(\kappa W) \right) A - \left(\frac{i\zeta}{\kappa v} \right) \sinh(\kappa W) B \right], \quad (\text{B22})$$

$$G = e^{-ikW} \left[\left(\cosh(\kappa W) - \left(\frac{iE}{\kappa v} \right) \sinh(\kappa W) \right) B + \left(\frac{i\zeta}{\kappa v} \right) \sinh(\kappa W) A \right]. \quad (\text{B23})$$

Here we used relations

$$\frac{\alpha^2 + \beta^2}{\alpha^2 - \beta^2} = \frac{-iE}{\kappa v}, \quad \frac{2\alpha\beta}{\alpha^2 - \beta^2} = \frac{-i\zeta}{\kappa v}. \quad (\text{B24})$$

Similarly to the consideration in Appendix A, one can find the transmission and reflection amplitudes. Setting

$A = 0$ (switching off S_L) leads to

$$t_R = \frac{B}{G} = \frac{(\kappa v) e^{ikW}}{(\kappa v) \cosh(\kappa W) - iE \sinh(\kappa W)}, \quad (\text{B25})$$

$$r_R = \frac{H}{G} = -\frac{i\zeta \sinh(\kappa W) e^{2ikW}}{(\kappa v) \cosh(\kappa W) - iE \sinh(\kappa W)}. \quad (\text{B26})$$

Setting $G = 0$ (switching off S_R), one gets

$$t_L = \frac{H}{A} = \frac{(\kappa v) e^{ikW}}{(\kappa v) \cosh(\kappa W) - iE \sinh(\kappa W)}, \quad (\text{B27})$$

$$r_L = \frac{B}{A} = -\frac{i\zeta \sinh(\kappa W)}{(\kappa v) \cosh(\kappa W) - iE \sinh(\kappa W)}. \quad (\text{B28})$$

One checks that the unitarity of the \mathcal{S} -matrix is satisfied. The transmission function

$$\mathcal{T}_{\text{wqpc}}(E) = |t_L|^2 = \left(1 + \zeta^2 \sinh^2(\kappa W) / (\kappa v)^2\right)^{-1} \quad (\text{B29})$$

can be represented as Eq. (14).

Appendix C: Point limit of transmission function in conventional quantum mechanics

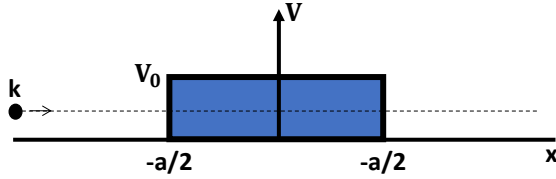


Figure 13. Rectangular potential barrier.

Here we discuss the point limit of a rectangular barrier for a conventional quantum particle with dispersion relation $p^2/(2m)$. For brevity of notation, we put $\hbar = 1$ in this section.

Consider Hamiltonian

$$H = \int_{-\infty}^{+\infty} dx \left(-\psi^\dagger(x) \frac{\partial_x^2}{2m} \psi(x) + V(x) \psi^\dagger(x) \psi(x) \right), \quad (\text{C1})$$

where the potential

$$V(x) = \begin{cases} V_0, & |x| < \frac{a}{2}, \\ 0, & |x| > \frac{a}{2}. \end{cases} \quad (\text{C2})$$

For energies $E \leq V_0$ this potential represents a potential barrier for a quantum particle, cf. Fig. 13. The probability for a particle to be transmitted through the barrier is given by [47, Section 1.3.11]

$$\mathcal{T}_{\text{rect}}(E) = \left(1 + \frac{\sinh^2(\kappa a)}{4} \left[\frac{\kappa^2 + k^2}{k\kappa} \right]^2\right)^{-1}, \quad (\text{C3})$$

where $k = \sqrt{2mE}$, and $\kappa = \sqrt{2m(V_0 - E)}$.

Putting $V_0 = \alpha/a$ and taking the limit $a \rightarrow 0$ makes the potential a delta-function barrier: $V(x) = \alpha\delta(x)$. The transmission probability for the delta potential is given by [47, Section 1.3.12]

$$\mathcal{T}_{\text{delta}}(E) = \left(1 + [m\alpha/k]^2\right)^{-1}. \quad (\text{C4})$$

This expression can be reproduced by taking the limit of $\mathcal{T}_{\text{rect}}(E)$. Indeed, in the limit $V_0 = \alpha/a$, $a \rightarrow 0$,

$$\kappa \approx \sqrt{2mV_0} = \sqrt{2m\alpha/a} \rightarrow \infty, \quad (\text{C5})$$

$$\kappa a \approx \sqrt{2m\alpha a} \rightarrow 0, \quad (\text{C6})$$

$$\sinh(\kappa a) \approx \kappa a, \quad (\text{C7})$$

so that

$$\begin{aligned} \frac{\sinh^2(\kappa a)}{4} \left[\frac{\kappa^2 + k^2}{k\kappa} \right]^2 &\approx \frac{(\kappa a)^2}{4} \left[\frac{\kappa}{k} \right]^2 \\ &= \left[\frac{\kappa^2 a}{2k} \right]^2 = \left[\frac{m\alpha}{k} \right]^2. \end{aligned} \quad (\text{C8})$$

Therefore,

$$\lim_{a \rightarrow 0, V_0 = \alpha/a} \mathcal{T}_{\text{rect}}(E) = \mathcal{T}_{\text{delta}}(E). \quad (\text{C9})$$

This consideration shows that in the conventional quantum-mechanical problem with dispersion relation $p^2/(2m)$, the properties of a delta-barrier can be obtained from the properties of the narrow and high rectangular potential. Contrast this to the consideration of Sec. IV: the transmission function $\mathcal{T}_{\text{pqp}}(E)$ obtained from the point-QPC model (which corresponds to delta-tunneling at $x = 0$) does not coincide with the point limit of the transmission functions obtained from the wide-QPC and long-QPC models ($\mathcal{T}_{\text{wqpc}}(E)$ and $\mathcal{T}_{\text{lqpc}}(E)$). It would be interesting to check whether taking a non-linear edge dispersion in the point-, wide-, and long-QPC models would fix this discrepancy.

Appendix D: The role of edge velocity

In the main text (cf. Fig. 8), we have discussed the results for the transmission function behavior when using realistic parameters. We chose the value of velocity $v = 2 \times 10^4$ m/s for consideration there. Here we demonstrate the effect of velocity value. In experiments, values in the range of $v = 10^4$ – 10^6 m/s have been reported [12, 40–46].

We take the same parameters as in the main text and plot the transmission function for $v = 2 \times 10^3$, 2×10^4 , and 2×10^5 m/s. The results are presented in Fig. 14. One observes that velocity strongly affects the predictions of the wide-QPC model for all values of \mathcal{T}_0 . The point-QPC prediction is unaffected as it is equal to \mathcal{T}_0 for all energies. Similarly, the long-QPC model is also hardly affected since its transmission function is fully determined by \mathcal{T}_0 when $E \ll \Delta$. This shows that whenever energy dependence of the transmission function is significant, the edge state velocity is an important factor.

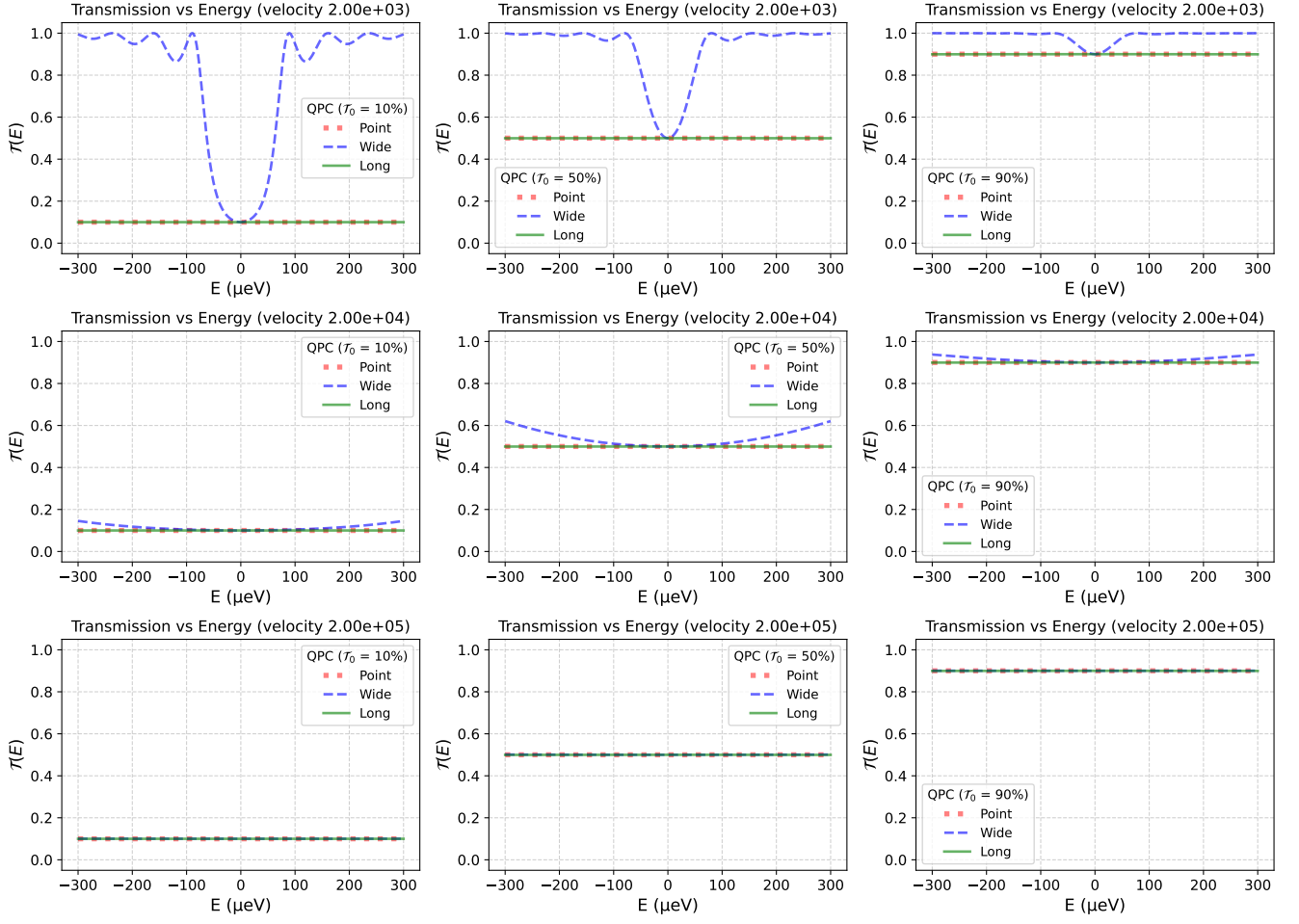


Figure 14. The predictions of the point-QPC, wide-QPC, and long-QPC models for the transmission function $\mathcal{T}(E)$ several values of edge velocity v . The models that predict insignificant energy dependence of $\mathcal{T}(E)$ are also not sensitive to the velocity. By contrast, whenever the energy dependence of transmission function is noticeable (in this energy range, wide-QPC model only), velocity strongly affects the predictions.

-
- [1] K. von Klitzing, Quantum hall effect: Discovery and application, *Annual Review of Condensed Matter Physics* **8**, 13 (2017).
- [2] R. B. Laughlin, Anomalous quantum hall effect - an incompressible quantum fluid with fractionally charged excitations, *Physical Review Letters* **50**, 1395 (1983).
- [3] V. J. Goldman and B. Su, Resonant tunneling in the quantum hall regime: Measurement of fractional charge, *Science* **267**, 1010 (1995).
- [4] L. Saminadayar, D. C. Glatthli, Y. Jin, and B. Etienne, Observation of the $e/3$ fractionally charged Laughlin quasiparticle, *Physical Review Letters* **79**, 2526 (1997).
- [5] R. De-Picciotto, M. Reznikov, M. Heiblum, V. Umansky, G. Bunin, and D. Mahalu, Direct observation of a fractional charge, *Nature* **389**, 162 (1997).
- [6] M. Dolev, M. Heiblum, V. Umansky, A. Stern, and D. Mahalu, Observation of a quarter of an electron charge at the $\nu = 5/2$ quantum hall state, *Nature* **452**, 829 (2008).
- [7] J. Martin, S. Ilani, B. Verdenne, J. Smet, V. Umansky, D. Mahalu, D. Schuh, G. Abstreiter, and A. Yacoby, Localization of fractionally charged quasi-particles, *Science* **305**, 980 (2004).
- [8] V. Venkatachalam, A. Yacoby, L. Pfeiffer, and K. West, Local charge of the $\nu = 5/2$ fractional quantum hall state, *Nature* **469**, 185 (2011).
- [9] M. Kapfer, P. Roulleau, M. Santin, I. Farrer, D. A. Ritchie, and D. C. Glatthli, A Josephson relation for fractionally charged anyons, *Science* **363**, 846 (2019).
- [10] R. Bisognin, H. Bartolomei, M. Kumar, I. Safi, J.-M. Berroir, E. Bocquillon, B. Placais, A. Cavanna, U. Gennser, Y. Jin, and G. Feve, Microwave photons emitted by fractionally charged quasiparticles, *Nature Communications* **10**, 1708 (2019).
- [11] D. Arovas, J. R. Schrieffer, and F. Wilczek, Fractional statistics and the quantum hall effect, *Physical Review Letters* **53**, 722 (1984).
- [12] J. Nakamura, S. Liang, G. C. Gardner, and M. J. Manfra, Direct observation of anyonic braiding statistics, *Nature Physics* **16**, 931 (2020).
- [13] H. Bartolomei, M. Kumar, R. Bisognin, A. Marguerite, J.-M. Berroir, E. Bocquillon, B. Placais, A. Cavanna, Q. Dong, U. Gennser, Y. Jin, and G. Feve, Fractional statistics in anyon collisions, *Science* **368**, 173 (2020), data: <https://zenodo.org/record/3692704>.
- [14] J. young M Lee, C. Hong, T. Alkalay, N. Schiller, V. Umansky, M. Heiblum, Y. Oreg, and H.-S. Sim, Partitioning of diluted anyons reveals their braiding statistics, *Nature* **617**, 277 (2023).
- [15] P. Glidic, O. Maillet, A. Aassime, C. Piquard, A. Cavanna, U. Gennser, Y. Jin, A. Anthore, and F. Pierre, Cross-correlation investigation of anyon statistics in the $\nu = 1/3$ and $2/5$ fractional quantum hall states, *Physical Review X* **13**, 011030 (2023).
- [16] M. Ruelle, E. Frigerio, J.-M. Berroir, B. Placais, J. Rech, A. Cavanna, U. Gennser, Y. Jin, and G. Feve, Comparing fractional quantum hall Laughlin and Jain topological orders with the anyon collider, *Physical Review X* **13**, 011031 (2023).
- [17] M. Ruelle, E. Frigerio, E. Baudin, J.-M. Berroir, B. Placais, B. Gremaud, T. Jonckheere, T. Martin, J. Rech, A. Cavanna, U. Gennser, Y. Jin, G. Menard, and G. Feve, Time-domain braiding of anyons, *Science* **389**, 10.1126/science.adm7695 (2025).
- [18] C. Nayak, S. H. Simon, A. Stern, M. Freedman, and S. D. Sarma, Non-abelian anyons and topological quantum computation, *Reviews of Modern Physics* **80**, 1083 (2008).
- [19] X. G. Wen, *Quantum Field Theory of Many-Body Systems: From the Origin of Sound to an Origin of Light and Electrons: From the Origin of Sound to an Origin of Light and Electrons* (OUP Oxford, 2004).
- [20] A. Veillon, C. Piquard, P. Glidic, Y. Sato, A. Aassime, A. Cavanna, Y. Jin, U. Gennser, A. Anthore, and F. Pierre, Observation of the scaling dimension of fractional quantum hall anyons, *Nature* **632**, 517 (2024).
- [21] R. Guerrero-Suarez, A. Suresh, T. Maiti, S. Liang, J. Nakamura, G. Gardner, C. Chamon, and M. Manfra, Universal anyon tunneling in a chiral Luttinger liquid, *arXiv:2502.20551* (2025).
- [22] N. Schiller, T. Alkalay, C. Hong, V. Umansky, M. Heiblum, Y. Oreg, and K. Snizhko, Scaling tunnelling noise in the fractional quantum hall effect tells about renormalization and breakdown of chiral Luttinger liquid, *arXiv:2403.17097* (2024).
- [23] X.-G. Wen, Edge transport properties of the fractional quantum hall states and weak-impurity scattering of a one-dimensional charge-density wave, *Physical Review B* **44**, 5708 (1991).
- [24] P. Fendley, A. W. W. Ludwig, and H. Saleur, Exact nonequilibrium dc shot noise in Luttinger liquids and fractional quantum hall devices, *Physical Review Letters* **75**, 2196 (1995).
- [25] I. P. Levkivskyi, A. Boyarsky, J. Frohlich, and E. V. Sukhorukov, Mach-Zehnder interferometry of fractional quantum hall edge states, *Physical Review B* **80**, 045319 (2009).
- [26] T. Morel, J.-Y. M. Lee, H.-S. Sim, and C. Mora, Fractionalization and anyonic statistics in the integer quantum hall collider, *Physical Review B* **105**, 075433 (2022).
- [27] N. Schiller, Y. Oreg, and K. Snizhko, Extracting the scaling dimension of quantum hall quasiparticles from current correlations, *Physical Review B* **105**, 165150 (2022).
- [28] B. Rosenow and B. I. Halperin, Braids and beams: Exploring fractional statistics with mesoscopic anyon colliders, *arXiv:2510.04319* (2025).
- [29] L. P. Pryadko, E. Shimshoni, and A. Auerbach, Coulomb interactions and delocalization in quantum hall constrictions, *Physical Review B* **61**, 10929 (2000).
- [30] E. Papa and A. H. MacDonald, Interactions suppress quasiparticle tunneling at Hall bar constrictions, *Physical Review Letters* **93**, 126801 (2004), Coulomb interaction between two edges of the QPC and between the edge on the two sides of the split gates renormalizes the scaling dimension in tunnelling experiments.
- [31] G. Yang and D. E. Feldman, Influence of device geometry on tunneling in the $\nu = 5/2$ quantum hall liquid, *Physical Review B* **88**, 085317 (2013).
- [32] J. C. Y. Teo and C. L. Kane, From Luttinger liquid to non-abelian quantum hall states, *Physical Review B* **89**, 085101 (2014).
- [33] Y. V. Nazarov and Y. M. Blanter, *Quantum Transport*

- (Cambridge University Press, 2009).
- [34] M. Buttiker, Absence of backscattering in the quantum hall effect in multiprobe conductors, *Physical Review B* **38**, 9375 (1988).
 - [35] T. Martin and R. Landauer, Wave-packet approach to noise in multichannel mesoscopic systems, *Physical Review B* **45**, 1742 (1992).
 - [36] M. Filippone and P. W. Brouwer, Tunneling into quantum wires: Regularization of the tunneling hamiltonian and consistency between free and bosonized fermions, *Physical Review B* **94**, 235426 (2016).
 - [37] C. W. Groth, M. Wimmer, A. R. Akhmerov, and X. Waintal, Kwant: a software package for quantum transport, *New Journal of Physics* **16**, 063065 (2014).
 - [38] P. Fendley, A. W. W. Ludwig, and H. Saleur, Exact nonequilibrium transport through point contacts in quantum wires and fractional quantum hall devices, *Physical Review B* **52**, 8934 (1995).
 - [39] P. Fendley and H. Saleur, Nonequilibrium dc noise in a luttinger liquid with an impurity, *Physical Review B* **54**, 10845 (1996).
 - [40] D. T. McClure, Y. Zhang, B. Rosenow, E. M. Levenson-Falk, C. M. Marcus, L. N. Pfeiffer, and K. W. West, Edge-state velocity and coherence in a quantum hall fabry-perot interferometer, *Physical Review Letters* **103**, 206806 (2009).
 - [41] H. Kamata, T. Ota, K. Muraki, and T. Fujisawa, Voltage-controlled group velocity of edge magnetoplasmon in the quantum hall regime, *Physical Review B* **81**, 085329 (2010).
 - [42] N. Kumada, H. Kamata, and T. Fujisawa, Edge magnetoplasmon transport in gated and ungated quantum hall systems, *Physical Review B* **84**, 045314 (2011).
 - [43] M. Kataoka, N. Johnson, C. Emary, P. See, J. Griffiths, G. Jones, I. Farrer, D. Ritchie, M. Pepper, and T. Janssen, Time-of-flight measurements of single-electron wave packets in quantum hall edge states, *Physical Review Letters* **116**, 126803 (2016).
 - [44] I. Gurman, R. Sabo, M. Heiblum, V. Umansky, and D. Mahalu, Dephasing of an electronic two-path interferometer, *Physical Review B* **93**, 121412(R) (2016).
 - [45] J. Nakamura, S. Fallahi, H. Sahasrabudhe, R. Rahman, S. Liang, G. C. Gardner, and M. J. Manfra, Aharonov–bohm interference of fractional quantum hall edge modes, *Nature Physics* **15**, 563 (2019).
 - [46] H. Weldeyesus, T. Patlatiuk, Q. Chen, C. P. Scheller, A. Yacoby, L. N. Pfeiffer, K. W. West, and D. M. Zumbuhl, Edge state selective measurement of quantum hall dispersions, *arXiv:2507.07905* (2025).
 - [47] Y. B. Band and Y. Avishai, Introduction to quantum mechanics, in *Quantum Mechanics with Applications to Nanotechnology and Information Science* (Elsevier, 2013) pp. 1–59.